LETTERS
PUBLISHED ONLINE: 12 AUGUST 2012 | DOI: 10.1038/NMAT3403
nature materials

Van der Waals interactions at metal/organic interfaces at the single-molecule level

Sriharsha V. Aradhya[1], Michael Frei[1], Mark S. Hybertsen[2]* and L. Venkataraman[1]*

Van der Waals (vdW) interaction, and its subtle interplay with chemically specific interactions and surface roughness at metal/organic interfaces, is critical to the understanding of structure–function relations in diverse areas, including catalysis, molecular electronics and self-assembly[1–3]. However, vdW interactions remain challenging to characterize directly at the fundamental, single-molecule level both in experiments and in first principles calculations with accurate treatment of the non-local, London dispersion interactions. In particular, for metal/organic interfaces, efforts so far have largely focused on model systems consisting of adsorbed molecules on flat metallic surfaces with minimal specific chemical interaction[4–9]. Here we show, through measurements of single-molecule mechanics, that pyridine derivatives[10,11] can bind to nanostructured Au electrodes through an additional binding mechanism beyond the chemically specific N–Au donor–acceptor bond. Using density functional theory simulations we show that vdW interactions between the pyridine ring and Au electrodes can play a key role in the junction mechanics. These measurements thus provide a quantitative characterization of vdW interactions at metal/organic interfaces at the single-molecule level.

In this work we probe bond rupture forces and junction stiffness in single-molecule junctions using a home-built conducting atomic force microscope (AFM). Single-molecule junctions are formed with 4,4'-bipyridine (BP) or 1,2-bis(4-pyridyl)ethylene (BPE) molecules bound between a Au substrate and a Au-coated cantilever (Fig. 1a). Measurements of current through the junction under an applied bias allow us to determine the junction conductance while simultaneous measurements of cantilever deflection relate to the force applied across the junction (see Methods). Figure 1b shows the simultaneously measured conductance (upper panel) and force (lower panel) during the evolution of an Au quantum point-contact under elongation. The conductance trace shows plateaux at integer multiples of G_0 ($2e^2/h$, quantum of conductance) as the Au point-contact thins and ruptures. When the same measurements are carried out in the presence of BP or BPE molecules on the Au substrate, additional conductance plateaux are seen in the traces at conductance values that are characteristic of a single Au–molecule–Au junction. Previous work has shown that pyridine-terminated molecules bind to the Au electrodes in two distinct geometries, each with a characteristic conductance dictated primarily by the separation between the two electrodes[10–12]. A high-conductance junction (BP_H or BPE_H) is formed when the electrode separation is smaller than the length of the molecule. On elongation, this junction can rearrange to form a low-conductance junction (BP_L or BPE_L). The upper panels of Fig. 1c,d show the conductance evolution of an Au point-contact in the presence of BP and BPE as a function of elongation. We see a plateau around $1G_0$, followed by a sequence of two plateaux at lower conductance values, indicating that the Au single-atomic contact ruptures to form a BP_H or BPE_H junction, which rearranges to a BP_L or BPE_L junction. The distance over which the junction remains in the high-conductance state is highlighted in the upper panels of Fig. 1c,d and defines the high-conductance step length. Statistically, we find signatures of the high-conductance junctions in ~80% of the measured traces, and these features always precede the low-conductance junctions, when present. BP_H and BPE_H can also rupture on elongation without switching to their respective low-conductance states. Once the Au–molecule–Au junction is fully ruptured, no current is measured between the tip and surface.

The simultaneously acquired force traces (lower panels of Fig. 1b–d) show repeated saw-tooth patterns, where each linear force ramp is indicative of elastic stretching of the junction with its characteristic stiffness (the slope of this ramp), whereas the drops in forces correspond to abrupt events involving bond rupture and junction rearrangements[13–16]. These force traces also clearly demonstrate the typical rupture events that occur when the BP_H (BPE_H) junction switches to a BP_L (BPE_L) junction. Although most abrupt force drops coincide with changes in conductance, we find that structural rearrangements frequently occur during the elongation of the BP_H and BPE_H junctions, without significant conductance variations, as illustrated in Fig. 1c,d. Several distinct load-rupture saw-tooth events are seen in these force traces during the span of one BP_H/BPE_H conductance plateau. The distance over which these junctions rearrange before the final load/rupture event is highlighted in the lower panels of Fig. 1c,d and defines the rearrangement length. Although it has been common to assume that a conductance plateau corresponds to the stretching of a single bonding motif[17,18], these observations demonstrate that conductance plateaux can span a sequence of local junction structures[19]. Here the simultaneously measured force provides an independent local probe of structural rearrangement.

We measure and analyse thousands of individual force and simultaneously acquired conductance measurements to determine junction rupture forces (force drops in individual traces) and junction stiffness (slope of the force ramps). We use conductance as the fingerprint and focus on three distinct regimes during junction elongation: Au single-atomic contacts, low-conductance BP_L or BPE_L junctions and high-conductance BP_H or BPE_H junctions that rupture to an open junction (see Methods for details). Histograms of force and stiffness values for these three cases are shown in Fig. 2a,b, respectively. We find that Au single-atomic contacts rupture with an average force of 1.5 nN and have an average

[1]Department of Applied Physics and Applied Mathematics, Columbia University, New York, New York 10027, USA, [2]Center for Functional Nanomaterials, Brookhaven National Laboratory, Upton, New York 11973, USA. *e-mail: mhyberts@bnl.gov; lv2117@columbia.edu.

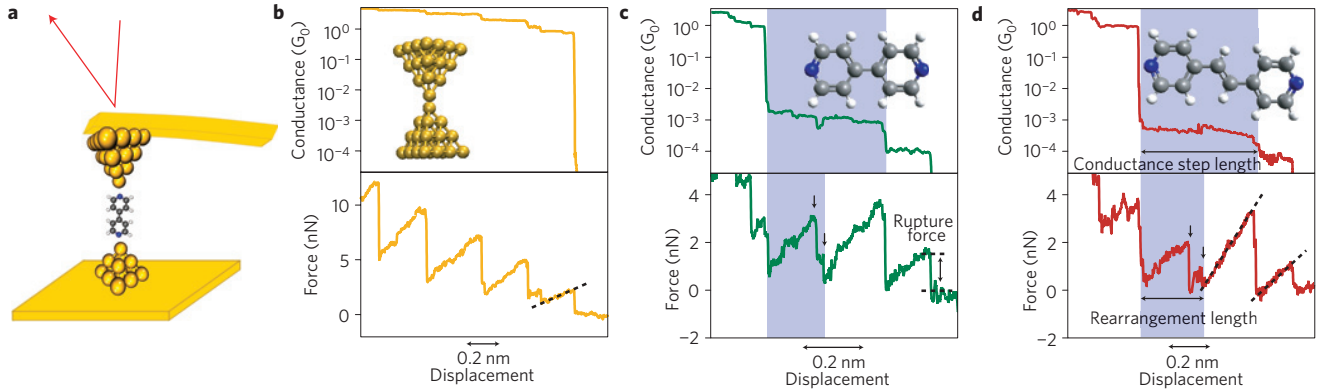

Figure 1 | Simultaneous measurement of single-molecule conductance and force. a, Schematic representation of a BP junction formed between a gold-coated AFM cantilever and a gold substrate. Au, C, H and N atoms are shown in yellow, grey, white and blue, respectively. **b**–**d**, Experimentally measured conductance (upper panel) and corresponding simultaneously acquired force (lower panel) sample traces during junction elongation for clean Au (**b**), BP (**c**) and BPE (**d**) junctions. Shaded areas in upper panels represent high-conductance molecular regimes. In the lower panels, the shaded areas represent structural rearrangements within high-conductance junctions that are clearly identified by abrupt force fluctuations (downward pointing arrows). Rupture force (demarcated by the dashed lines in **c**) is the drop in force when the junction ruptures to an open junction. The stiffness is the slope of the force ramp (as indicated by the dashed line fits in **b** and **d**) .

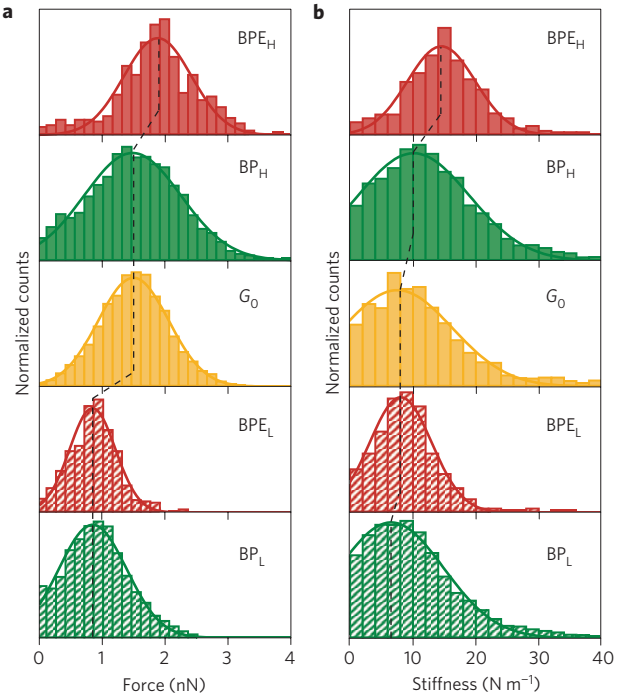

Figure 2 | Rupture force and stiffness of single-molecule junctions. **a**,**b**, Histograms of rupture forces (**a**) and effective stiffness (**b**) for BP_L (shaded green; mean rupture force $F_{rup} = 0.85 \pm 0.01$ nN, mean stiffness $K_{junc} = 6.7 \pm 0.1$ N m^{-1}, number of measurements represented $N = 7,763$), BPE_L (shaded red; $F_{rup} = 0.85 \pm 0.01$ nN, $K_{junc} = 8.2 \pm 0.1$ N m^{-1}, $N = 501$), Au (yellow; $F_{rup} = 1.50 \pm 0.01$ nN, $K_{junc} = 7.7 \pm 0.3$ N m^{-1}, $N = 2,346$), BP_H (green; $F_{rup} = 1.48 \pm 0.01$ nN, $K_{junc} = 10.2 \pm 0.2$ N m^{-1}, $N = 4,118$) and BPE_H (red; $F_{rup} = 1.88 \pm 0.02$ nN, $K_{junc} = 14.6 \pm 0.2$ N m^{-1}, $N = 530$) junctions. Solid lines are Gaussian fits to the data and dashed lines connecting the peaks of the distributions are provided as visual guides.

effective stiffness of 8 N m^{-1}, in excellent agreement with previously published results[13–15]. The errors in the peak positions of force and stiffness are dominated by the experimental uncertainty of AFM cantilever calibrations (see Supplementary Information). The widths of the distributions, on the other hand, are representative of intrinsic junction-to-junction variations, which are found even in measurements carried out at 4.2 K in vacuum[13,14]. The rupture force and stiffness are extremely sensitive to the details of the sampled potential energy landscapes[15,16]. The measurements of sufficiently large datasets, as presented here, provide a statistically meaningful comparison between junctions that are different both chemically and physically.

The low-conductance BP_L and BPE_L junctions both rupture at ~0.8 nN, in excellent agreement with previously published experimental measurements[14,20] and adiabatic trajectory calculations performed with methods based on density functional theory (DFT) for BP_L junctions[14,16]. These junctions typically show a single load-rupture saw-tooth in force, and exhibit a shorter conductance step (95th percentile length is ~0.1 nm) than the high-conductance junctions, consistent with the stretching and rupture of the N–Au bond. Both the BP_L and BPE_L junctions have a similar stiffness (7 and 8 N m^{-1} respectively), close to that of Au single-atomic contacts (8 N m^{-1}). Junction stiffness, in a simplified picture, corresponds to the effective spring constant of the entire metal–molecule–metal junction, where each bond can be modelled as a spring. Within this picture, the stiffness of a Au–molecule–Au junction, where the molecule is bonded to only one Au atom on each electrode apex, can only be equal to or smaller than that of an Au single-atomic contact. The stiffness measurements for BP_L and BPE_L are therefore consistent with geometries where the molecule bridges the apex of both electrodes through the formation of an Au–N donor–acceptor bond[11,14,16]. In contrast, the high-conductance BP_H and BPE_H junctions have an average rupture force of 1.5 and 1.9 nN, which is equal to or larger than that of the single Au atomic contact. Although the average value for the BP_H junction is similar to that for the single Au contact, the larger average rupture force measured with BPE_H rules out an explanation of these experimental measurements based on Au–Au bond rupture. As both molecules have the same terminal groups, the significantly larger rupture forces measured here for the high-conductance junctions demonstrate a binding mechanism that goes beyond the specific Au–N bond interaction.The measured stiffnesses for BP_H and BPE_H junctions are 10 N m^{-1} and 15 N m^{-1} respectively, both higher than the stiffness of the single Au atom contacts. Considered within the spring model discussed above, these large stiffness values imply a significantly different molecule–electrode interaction, involving an additional binding mechanism.

To understand better the structure of these high-conductance junctions we focus now on the structural rearrangement signatures

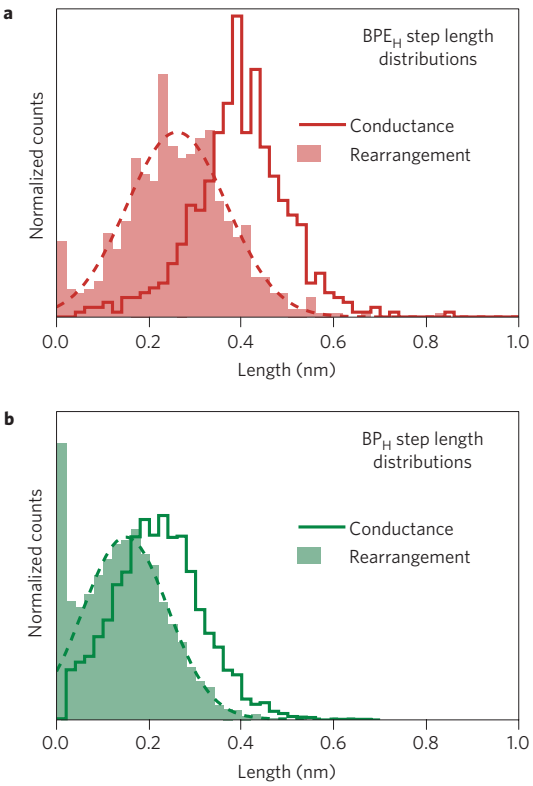

Figure 3 | Structural rearrangements in high-conductance junctions. **a**,**b**, Conductance step length and rearrangement length distributions for BPE_H (**a**) and BP_H (**b**) junctions show that only a small fraction of junctions are comprised of a single stable structure during elongation (counts near zero rearrangement length). Dashed lines are Gaussian fits to the non-zero portions of rearrangement length distributions.

measured in the force trace in BP_H and BPE_H junctions. We see saw-tooth features in addition to the final force drop due to rupture or switching of the junction to the low-conductance state (lower panels of Fig. 1c,d). These additional events in force indicate that these high-conductance junctions undergo a sequence of structural rearrangements, with little impact on the conductance. The final stable high-conductance structure exists only over a relatively small fraction of the conductance plateau, given by the difference between the conductance step length and the rearrangement length as defined above. In Fig. 3, we show histograms of the conductance step lengths and the rearrangement lengths for BP_H and BPE_H junctions. These distributions, which are peaked at 0.15 nm and 0.26 nm for BP_H and BPE_H respectively, show that a large fraction of the high-conductance steps (~88% of BP_H and ~95% of BPE_H) undergo structural rearrangements. Although these rearrangements could be due to chain formation in the Au electrodes[21], the high stiffness measured in these structures rules out this explanation. This shows that the molecule is changing its attachment point on the electrode under stress and/or causes the motion of local Au atoms[22], consistent with the fact that the rearrangement length scales with the length of the molecule[19].

Taken together, the rupture force, stiffness and rearrangement length measurements allow us to deduce a model for junction formation and evolution as illustrated in Fig. 4a. An Au quantum point-contact is first formed between two electrode surfaces. On rupture, the electrode surfaces present both undercoordinated Au sites that support specific N–Au donor–acceptor bonds, as well as larger Au structures[23] which interact with the pyridine rings through non-specific vdW interactions (both electrostatic and non-local London dispersion interactions). These conditions are optimal for the formation of a high-conductance junction. As this junction evolves under stress, it can either rupture or switch into the low-conductance junction. This is consistent with past work where it was shown that the high-conductance junction results when the electrode separation is smaller than the molecule length, whereas low-conductance junctions seem to occur with the molecule bridging the apex atoms on the electrodes[11].

To understand the mechanics in more detail, we use DFT-based calculations to explore several bonding scenarios while also including the role of the dispersion interactions, the non-local correlation contribution not captured in typical DFT implementations, within the DFT-D2 approach[24] (see Methods). We first consider the impact of dispersion interactions on the mechanics of low-conductance junctions. Previous DFT-based calculations have focused on the chemically specific N–Au donor–acceptor bond in idealized BP_L junctions[14,16]. We revisit several prototypical structures for BP bound to a single Au-atom (see Supplementary Information) and compare DFT results with those that include dispersion interactions. We find that the inclusion of the dispersion interactions leads to small increases in the bond rupture force (less than 0.2 nN). In these geometries the specific chemical interaction of the donor–acceptor bond dominates and hence gradient corrected DFT calculations[25] without dispersion interactions are sufficient to characterize the binding.

To model the high-conductance geometry we consider the electrode surface that is illustrated in Fig. 4b, where the rough electrode surface is modelled by an asperity consisting of a two-atom high ridge. The BP molecule is bonded to an adatom near a two-layer ridge. The tilt of the BP molecule backbone models the constraint of bonding to the other electrode (implicit here and simulated by control of the position of the upper N atom). The chemical N–Au donor–acceptor bond strength is found to be about 1 eV. Furthermore, owing to the proximity of the ridge structure, the dispersion interaction contributes an additional 0.8 eV to the binding energy. The junction elongation is simulated by moving the molecule vertically upwards in increments of 0.01 Å, followed by a relaxation with the upper (unbound) N fixed (Fig. 4b–f). After an elongation of 0.16 nm there is an abrupt structural rearrangement: the molecule pulls the adatom to an adjacent hollow site while maintaining the Au–N bond (Fig. 4c). The calculated force drop for this event is about 0.8 nN, consistent with the force drops accompanying structural rearrangements in the experiment (Fig. 1c,d). As the junction is elongated, the ring passes the edge of the asperity and the loss of vdW interaction energy contributes significantly to the maximum sustained force of 1.8 nN (Fig. 4d), in good agreement with the experimental results. The dispersion contributions account for 1 nN for this specific trajectory. Overall, the contribution of non-specific, vdW interactions (electrostatic plus dispersion) to the maximum sustained force is sensitive to the interplay between the local N–Au bond elongation during rupture and the coordination of the ring to the ridge structure; the vdW contribution is probably between 0.4 to 1 nN (see Supplementary Fig. S7 and related discussion).

The key results of the calculations are twofold: in the low-conductance BP_L junctions, the dispersion contribution is minimal and in the high-conductance BP_H junctions, both chemically specific Au–N and vdW interactions need to be considered together to explain the experimentally measured rupture forces. For junctions with the longer BPE molecule, the specific chemical interactions are similar to BP, but the increased length can lead to more optimized vdW interactions of the pyridine rings with Au structures, longer sequences of structural rearrangement and to even larger rupture force and stiffness compared with BP, as observed in the experiment. Finally, the constrained geometry in Fig. 4c results in the N–Au bond being at a substantial angle to the

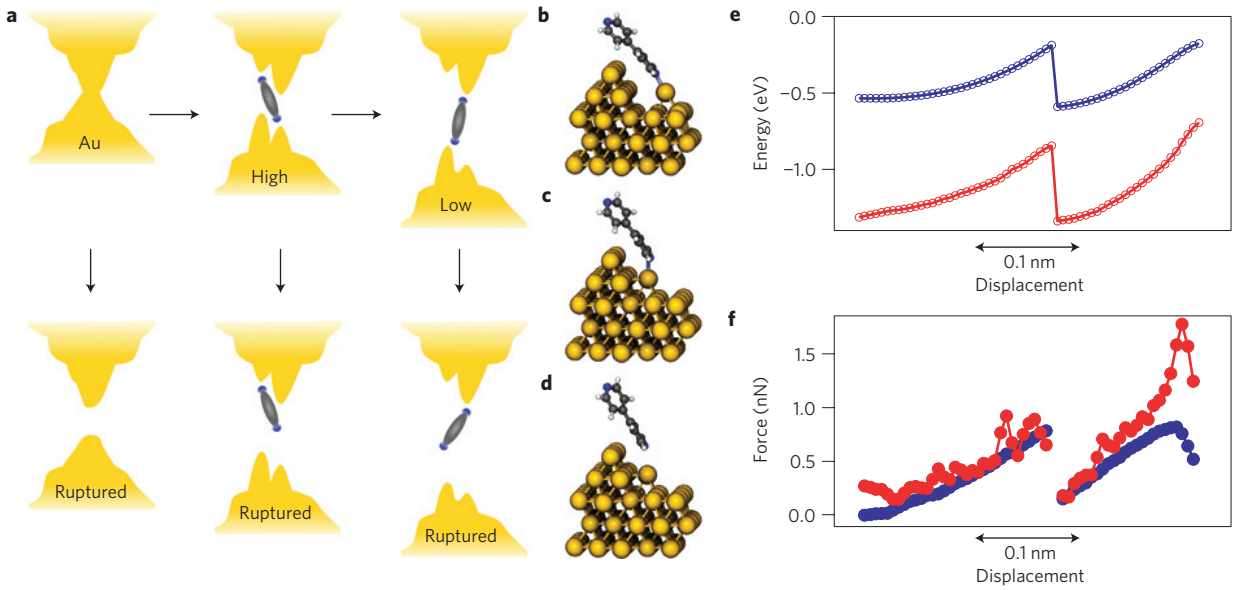

Figure 4 | Structural evolution during junction elongation. a, Schematic of structural evolution pathways deduced from experimental observations. In addition to rupture, the high-conductance junctions show structural rearrangement and switching to the low-conductance structures. **b**, Model structure suitable for DFT calculations in which the BP adopts a tilted configuration due to constraints of junction formation and in which a significant contribution from dispersion interactions of the aromatic ring with the atomic-scale roughness can be probed. **c**, On elongation, a structural rearrangement event that retains the specific Au–N bond is accompanied by a large force drop. **d**, Further elongation of the final stable structure results in the rupture of the Au–N bond. **e**,**f**, Calculated energies (**e**) and forces (**f**) with (red) and without (blue) inclusion of dispersion effects demonstrates the significant contributions from dispersion interactions. The electrode reference energy is taken to be the final electrode structure in **d**. The binding energy relative to the initial electrode structure in **b** is 0.45 eV stronger, giving an initial binding energy before rearrangement of 1.8 eV.

plane of the pyridine ring, consistent with a link structure that was previously proposed to explain the high-conductance junction[11]. Furthermore, the proximity of the C atoms in the pyridine ring to the top of the ridge structure (3.5 Å) facilitates enhanced electronic coupling[26] and is therefore expected to contribute to the higher conductance[22]. We have ruled out any appreciable mechanical stabilization due to specific Au–C bonding through control measurements with 4-phenylpyridine and 4-styrylpyridine molecules (see Supplementary Fig. S2). These molecules have the same molecular structure as BP and BPE respectively, except there is a nitrogen atom on only one side of the molecule to form specific N–Au bonds. Neither of these molecules show well-defined conductance plateaux, and force measurements with 4-styrylpyridine do not show any force saw-tooth events beyond the Au G_0 rupture. These results demonstrate that there are no independently formed Au–C bonds that are comparable in strength to the chemical Au–N interactions seen in these systems.

In summary, we have used an AFM to probe the interplay between specific Au–N and non-specific vdW interactions between the surface structure on the Au electrode and two pyridine-terminated molecules. Our results provide a unique quantitative measurement of the relative importance of these two types of interfacial interaction at the single-molecule level, in a regime where they are of comparable magnitude. These results will have particular impact on the drive to develop accurate theoretical treatment of vdW interactions at metal/molecule interfaces currently in a nascent stage, and especially to go beyond the simplest model systems of ideal, flat surfaces towards the treatment of the nanostructured metals that are critical to many areas of research and future technological applications.

Methods

Experimental methods. The experimental protocol for these measurements consists of repeatedly forming and breaking Au–Au contacts between the Au-coated tip of the AFM micro-cantilever and a molecule-covered Au substrate (the two 'electrodes'). Once a high-conductance contact is formed, with a conductance greater than $5G_0$ ($G_0 = 2e^2/h$), the two electrodes are pulled apart at a constant speed of 18 nm s^{-1} using a single-axis piezoelectric positioner, calibrated to 5% accuracy in displacement. A constant voltage bias(25 mV for Au and 75 mV for BP and BPE measurements) is applied between the tip and substrate in series with a fixed resistor while the current through the junction is measured. The cantilever deflection is measured simultaneously using AFM optical deflection techniques, which have been optimized to achieve a displacement resolution of ~2 pm r.m.s. We perform all the measurements under ambient conditions at room temperature. We collect 1,000–3,000 measurements without molecules (clean Au) with each tip and substrate used before depositing molecules by evaporation, to ensure the absence of contaminants in our set-up. The deposition of either BP or BPE (both from Sigma-Aldrich) was performed by evaporation onto Au-coated mica substrates.

Data analysis. For analysis we separately focus on Au G_0, BP_H/BPE_H and BP_L/BPE_L junctions. To characterize the rupture force of Au single-atom contacts we consider $1G_0$ conductance plateaux that evolve into a ruptured junction (Fig. 4a). The rupture force for BP_H/BPE_H is similarly characterized by considering high-conductance plateaux that result in ruptured junctions, while the switching force can also be extracted by considering the high-conductance plateaux that evolve into low-conductance junctions. As the low-conductance junctions always evolve to a ruptured junction, every measurement showing BP_L/BPE_L plateaux is included in the analysis. We use an automated algorithm to delineate conductance signatures from structural evolution, as detailed in the Supplementary Information. Briefly, the algorithm begins by locating a conductance plateau in the range of conductance which is of interest: G_0 (for Au) and high- or low-conductance molecular plateau (for either BP or BPE). Next, the algorithm finds all the force fluctuations that are higher than 0.25 nN (instrument force noise ~0.15 nN r.m.s.) over the displacement range corresponding to the conductance plateau of interest. These force signatures help isolate individual structures that undergo loading and rupture, which cannot be determined from the conductance trace alone (Fig. 2c,d). We can determine the bond rupture force by looking at the drop in the force trace of the last event. Finally, we perform a linear fit to the force ramp region of this last event, and thereby extract the junction stiffness after correcting for the small contribution from the relatively large, but finite spring constant of the cantilever (~50 N m^{-1}) that is in series with each junction. The number of measurements represented in the force and stiffness histograms is: Au G_0—2,346, BP_H—4,118, BP_L—7,763, BPE_H—530, and BPE_L—501. The means and their computed error from the Gaussian fits (~0.01–0.02 nN for the rupture force histograms and ~0.1–0.3 N m^{-1} for the stiffness histograms) are listed in the caption for Fig. 2.

DFT calculations. The BP interaction with the Au electrode was modelled with a periodic slab geometry consisting of three monolayers of (111)-oriented Au plus ad-structures and the molecule. The surface unit cell for the ridge plus adatom structure illustrated in Fig. 4 was 5×5. The vertical distance between the upper N atom and the bottom Au layer in the periodic supercell was at least 13 Å. During simulation, the two back layers atoms in the Au slab were held fixed with a bulk lattice parameter of 4.13 Å. All other degrees of freedom were relaxed until all forces were less than 0.01 eV $Å^{-1}$ for each structure. We focus on one side of the junction, considering only one N–Au link bond, and fix the position of the other N atom in the BP molecule to define a specific value of elongation. The junction was elongated in steps of 0.01 Å by shifting the BP molecule relative to the slab. Data is recorded for every 0.05 or 0.1 Å of shift, with a force criterion for structural relaxation enforced. To estimate the role of vdW interactions in the bond rupture process, the semi-empirical Grimme DFT-D2 approach[24] to correct the Perdew-Burke Ernzerhof (PBE) version of the generalized gradient approximation[27] as implemented in the Vienna Ab Initio Simulation Package[28] (VASP) has been employed, using C_6 and R_0 values of 422 eV $Å^6$ and 1.772 Å respectively[29], and a cutoff radius of 6 Å. Most of the calculations so far in the literature consider molecules on flat metal surfaces. We find a strong influence of the additional Au–Au interactions on the ad-structures (pyramid and ridge). Therefore, we use a perturbative approach, as has been done in other studies involving undercoordinated metal structures[30]. The structure is determined with PBE and the DFT-D2 model provides a correction to the total energy. Further description of the calculations, calibrations and results are provided in the Supplementary Information.

Received 3 May 2012; accepted 18 July 2012; published online 12 August 2012

References

1. Norskov, J. K., Bligaard, T., Rossmeisl, J. & Christensen, C. H. Towards the computational design of solid catalysts. *Nature Chem.* **1,** 37–46 (2009).
2. Moth-Poulsen, K. & Bjornholm, T. Molecular electronics with single molecules in solid-state devices. *Nature Nanotech.* **4,** 551–556 (2009).
3. Bartels, L. Tailoring molecular layers at metal surfaces. *Nature Chem.* **2,** 87–95 (2010).
4. Cunha, F. *et al.* Potential-induced phase transitions in 2,2'-bipyridine and 4,4'-bipyridine monolayers on Au(111) studied by *in situ* scanning tunneling microscopy and atomic force microscopy. *Langmuir* **12,** 6410–6418 (1996).
5. Wandlowski, T., Ataka, K. & Mayer, D. *In situ* infrared study of 4,4 '-bipyridine adsorption on thin gold films. *Langmuir* **18,** 4331–4341 (2002).
6. Mercurio, G. *et al.* Structure and energetics of Azobenzene on Ag(111): Benchmarking semiempirical dispersion correction approaches. *Phys. Rev. Lett.* **104,** 036102 (2010).
7. Tonigold, K. & Gross, A. Adsorption of small aromatic molecules on the (111) surfaces of noble metals: A density functional theory study with semiempirical corrections for dispersion effects. *J. Chem. Phys.* **132,** 224701 (2010).
8. Ruiz, V. G., Liu, W., Zojer, E., Scheffler, M. & Tkatchenko, A. Density-functional theory with screened van der Waals interactions for the modeling of hybrid inorganic–organic systems. *Phys. Rev. Lett.* **108,** 146103 (2012).
9. Li, G., Tamblyn, I., Cooper, V. R., Gao, H-J. & Neaton, J. B. Molecular adsorption on metal surfaces with van der Waals density functionals. *Phys. Rev. B* **85,** 121409 (2012).
10. Tam, E. S. *et al.* Single-molecule conductance of pyridine-terminated dithienylethene switch molecules. *ACS Nano* **5,** 5115–5123 (2011).
11. Quek, S. Y. *et al.* Mechanically controlled binary conductance switching of a single-molecule junction. *Nature Nanotech.* **4,** 230–234 (2009).
12. Hong, W. *et al.* Single molecular conductance of tolanes: Experimental and theoretical study on the junction evolution dependent on the anchoring group. *J. Am. Chem. Soc.* **134,** 2292–2304 (2011).
13. Rubio-Bollinger, G., Bahn, S. R., Agrait, N., Jacobsen, K. W. & Vieira, S. Mechanical properties and formation mechanisms of a wire of single gold atoms. *Phys. Rev. Lett.* **87,** 026101 (2001).
14. Frei, M., Aradhya, S. V., Koentopp, M., Hybertsen, M. S. & Venkataraman, L. Mechanics and chemistry: Single molecule bond rupture forces correlate with molecular backbone structure. *Nano Lett.* **11,** 1518–1523 (2011).
15. Sorensen, M. R., Brandbyge, M. & Jacobsen, K. W. Mechanical deformation of atomic-scale metallic contacts: Structure and mechanisms. *Phys. Rev. B* **57,** 3283–3294 (1998).
16. Stadler, R., Thygesen, K. & Jacobsen, K. Forces and conductances in a single-molecule bipyridine junction. *Phys. Rev. B* **72,** 241401 (2005).
17. Huang, Z. F., Xu, B. Q., Chen, Y. C., Di Ventra, M. & Tao, N. J. Measurement of current-induced local heating in a single molecule junction. *Nano Lett.* **6,** 1240–1244 (2006).
18. Tsutsui, M., Taniguchi, M. & Kawai, T. Atomistic mechanics and formation mechanism of metal-molecule-metal junctions. *Nano Lett.* **9,** 2433–2439 (2009).
19. Kamenetska, M. *et al.* Conductance and geometry of pyridine-linked single-molecule junctions. *J. Am. Chem. Soc.* **132,** 6817–6821 (2010).
20. Xu, B. Q., Xiao, X. Y. & Tao, N. J. Measurements of single-molecule electromechanical properties. *J. Am. Chem. Soc.* **125,** 16164–16165 (2003).
21. Yanson, A. I., Bollinger, G. R., van den Brom, H. E., Agrait, N. & van Ruitenbeek, J. M. Formation and manipulation of a metallic wire of single gold atoms. *Nature* **395,** 783–785 (1998).
22. Meisner, J. S. *et al.* A single-molecule potentiometer. *Nano Lett.* **11,** 1575–1579 (2011).
23. Ohnishi, H., Kondo, Y. & Takayanagi, K. Quantized conductance through individual rows of suspended gold atoms. *Nature* **395,** 780–783 (1998).
24. Grimme, S. Semiempirical GGA-type density functional constructed with a long-range dispersion correction. *J. Comput. Chem.* **27,** 1787–1799 (2006).
25. Bilic, A., Reimers, J. R. & Hush, N. S. Adsorption of pyridine on the gold(111) surface: Implications for 'alligator clips' for molecular wires. *J. Phys. Chem. B* **106,** 6740–6747 (2002).
26. Schneebeli, S. T. *et al.* Single-molecule conductance through multiple π–π-stacked benzene rings determined with direct electrode-to-benzene ring connections. *J. Am. Chem. Soc.* **133,** 2136–2139 (2011).
27. Perdew, J. P., Burke, K. & Ernzerhof, M. Generalized gradient approximation made simple. *Phys. Rev. Lett.* **77,** 3865–3868 (1996).
28. Kresse, G. & Furthmuller, J. Efficient iterative schemes for *ab initio* total-energy calculations using a plane-wave basis set. *Phys. Rev. B* **54,** 11169 (1996).
29. Sławińska, J., Dabrowski, P. & Zasada, I. Doping of graphene by a Au(111) substrate: Calculation strategy within the local density approximation and a semiempirical van der Waals approach. *Phys. Rev. B* **83,** 245429 (2011).
30. Kelkkanen, A. K., Lundqvist, B. I. & Norskov, J. K. Van der Waals effect in weak adsorption affecting trends in adsorption, reactivity, and the view of substrate nobility. *Phys. Rev. B* **83,** 113401 (2011).

Acknowledgements

This work was supported by the National Science Foundation (Career CHE-07-44185) and by the Packard Foundation. A portion of this work was performed using facilities in the Center for Functional Nanomaterials at Brookhaven National Laboratory and supported by the US Department of Energy, Office of Basic Energy Sciences, under contract number DE-AC02-98CH10886 (M.S.H.). L.V. acknowledges support from the NSF DMR-1122594.

Author contributions

Experiments were conceived by S.V.A. and L.V. and performed by S.V.A. and M.F. All calculations were performed by M.S.H. Data analysis was done by S.V.A., who co-wrote the paper with M.S.H. and L.V.

Additional information

Supplementary information is available in the online version of the paper. Reprints and permissions information is available online at www.nature.com/reprints. Correspondence and requests for materials should be addressed to M.S.H. or L.V.

Competing financial interests

The authors declare no competing financial interests.